IEEE Access
Multidisciplinary | Rapid Review | Open Access Journal

Received 12 August 2022, accepted 19 August 2022, date of publication 24 August 2022, date of current version 29 August 2022.

Digital Object Identifier 10.1109/ACCESS.2022.3201351

APPLIED RESEARCH

Design of a Wireless Drone Recharging Station and a Special Robot End Effector for Installation on a Power Line

DARIO STUHNE[1], (Graduate Student Member, IEEE), VIET DUONG HOANG[2], GORAN VASILJEVIC[1], (Member, IEEE), STJEPAN BOGDAN[1], (Senior Member, IEEE), ZDENKO KOVACIC[1], (Senior Member, IEEE), ANIBAL OLLERO[3], (Fellow, IEEE), AND EMAD SAMUEL MALKI EBEID[2], (Senior Member, IEEE)

[1]Laboratory for Robotics and Intelligent Control Systems (LARICS), Faculty of Electrical Engineering and Computing, University of Zagreb, 10000 Zagreb, Croatia
[2]SDU UAS Centre, MMMI, University of Southern Denmark, 5230 Odense, Denmark
[3]GRVC Robotics Laboratories, University of Seville, Camino de los Descubrimientos, 41092 Sevilla, Spain

Corresponding author: Dario Stuhne (dario.stuhne@fer.hr)

This work was supported by the project AERIAL COgnitive Integrated Multi-task Robotic System with Extended Operation Range and Safety (AERIAL CORE) funded by European Union's Horizon 2020 Research and Innovation Programme under Grant 871479.

ABSTRACT Drone autonomous operations near power lines are growing steadily and require innovative techniques to keep them on air. This paper presents a novel electromechanical recharging station that can be mounted on energized AC power line to charge the drone battery wirelessly without a need to modify the electrical infrastructure. The work shows a thorough analysis of the electrical and mechanical core components to build a flexible, lightweight and efficient recharging station that can be attached to a robotic arm. The work also discusses the recharging station design and its special robot end effector that mechanically couples the station with an aerial manipulator. Finally, the recharging station has been tested in the lab and in a real power line setup to validate its design and efficiency. The total achieved mass is 2300 grams with a harvesting efficiency of 77% at 250 A primary current.

INDEX TERMS Recharging station, energy harvesting, drone, end effector, power line, unmanned aerial vehicle, aerial robotic manipulation.

I. INTRODUCTION

Transmission power line maintenance and inspection are tasks required to reduce power losses and maintain the efficiency of the power system. These activities require a maintenance team to travel long distances, often difficult to reach by land, to detect potential defects in power lines and transmission towers. One of the methods to solve these problems is to use robots to perform such tasks. Examples of such robots are presented in [1], [2], and [3], where the robots need to be manually attached to the power line before starting the work. Recent developments in aerial manipulation robotics [4], [5], [6], [7], offer the possibility to perform autonomous or semi-autonomous inspection and maintenance tasks without the operator having to climb power line poles.

The major drawback of aerial systems is the limited amount of energy stored in their batteries, which severely limits their ability to be used over long periods of time or long distances. The solution to this problem is to install UAV (Unmanned Aerial Vehicle) recharging stations at strategic locations on transmission lines. When the UAV's battery level is low, it can land at the recharging station, recharge its batteries, and continue its mission until the next time it needs recharging. Such a system can operate continuously without requiring human intervention or an operator on site, and would allow energy companies to complete their infrastructure maintenance and inspection tasks more quickly and efficiently. The power needed for a recharging station to recharge

The associate editor coordinating the review of this manuscript and approving it for publication was Agustin Leobardo Herrera-May.

FIGURE 1. Illustration of AERIAL CORE project task to autonomously deploy the recharging station with a drone, an aerial manipulator, and a special robot end effector to increase the autonomy rate of drones power line inspection and monitoring.

an UAV could be obtained from power lines. Because aerial manipulators can operate on power lines, there is no need to shutoff the power while the task is being performed. This method also increases worker safety because they do not have to climb power line pylons.

The on-the-fly recharging capabilities are a key enabler for new and modernised applications. For instance, in the field of Internet of Things (IoT), drones are seen as a "thing" (i.e., Internet of Drones (IoD)) that can be continuously connected to the Internet to provide data to smart cities and societies. In [8], the work thoroughly examined the application status of surveillance drones in the context of smart cities, which are divided into seven categories: transportation, environment, infrastructure, object or people detection and tracking, disaster management, data collection, and other. Applications in these categories range from traffic monitoring to bridge and power line inspection to fire detection and 3D city modelling, etc. On the other hand, the IoT has enabled an immense proliferation of various digital devices with sensing and communication capabilities. In the context of smart cities, this means that heterogeneous sensor devices are placed in physically inaccessible areas at a given time and deployed in a very short time to measure and analyse contextual information [9], [10]. However, all application scenarios in [8] require some degree of energy autonomy to accomplish the task. Due to the widespread use of drones for communication purposes in smart cities, the proposed recharging station can alleviate the problem of limited autonomy of flying drones and completely redefine the proposed framework in [9].

Unlike existing UAV recharging stations, those for power lines must deal with several problems. One problem is the installation of the recharging station on the power line. The solution for the installation is to equip the aerial manipulator with a special end effector for the installation of the recharging station. In this way, the recharging station can be installed autonomously, without the need for manual installation. Once the recharging station is installed, it should be able to harvest energy from the power grid and transmit it to the drone. One method of harvesting energy from an active transmission line is to use a split-core current transformer. The advantage of such an approach is that energy can be harvested from only one current-carrying wire. Also, it is possible to envelop the wire while the core is split and then connect two sides of the core. To reduce the weight of the recharging station and make it suitable for installation by an aerial manipulator, the weight of the current transformer must be limited, which in turn means limiting the maximum power that can be drawn from the transmission line. To mitigate this problem, the recharging station can be equipped with an internal battery that can be charged slowly in the absence of the drone and discharged quickly in the presence of the drone to recharge the batteries. The internal battery ensures that the drone is recharged as quickly as possible. Power can be transmitted to the drone via a wireless charging circuit.

The AERIAL CORE[1] project aims to develop cognitive capabilities for aerial robot perception, teaming, aerial morphing, force interaction manipulation, and human collaboration to maintain and monitor large infrastructures with aerial robots [11]. This includes, among other things, the maintenance of power lines through aerial manipulation, which is unprecedented in terms of range and safety. One of the goals of the AERIAL CORE project is also to develop a UAV recharging station (Figure 1). This paper presents a novel recharging station developed as part of the AERIAL CORE project and suitable for use on high-voltage power lines, as well as a special robotic end effector used for its installation. The mechanical design of the recharging station ensures that the recharging station is attached to the transmission line and the split core current transformer is closed with a suitable single degree of freedom (SDoF) end effector, which is removed from the recharging station when installation is complete. The electrical design enables power harvesting from the power grid using the concept of maximum power point tracking (MPPT) to charge the station's internal battery, which is then used to power the wireless charging circuit for wireless charging of the drone.

The idea of building wireless recharging stations for drones is not new. A number of methods have been proposed to wirelessly charge drones, such as using laser power beams [12], microwaves and millimeter waves [13], [14], capacitive energy transfer [15], and inductive energy transfer [16], [17]. However, these studies have only developed techniques for drone charging and have not focused on specific applications. Therefore, the power source for recharging stations was not considered at any stage. For power line inspection, the authors in [18] had the idea of setting up recharging stations on poles that could draw power from power lines and then wirelessly charge drones. However, this study only described the conceptual design of the stations and did not deploy a full system. In [19], a solution is proposed where recharging stations are built on the top of high-voltage towers where the energy is harvested from solar panels. The main drawback of this approach is the modification of the poles to install the recharging systems. Another approach is presented in [20],

[1] https://aerial-core.eu/

where a 400 W recharging station was designed near the power pole, powered by a 200 VAC power source on the ground, to wirelessly charge drones. However, low-voltage power sources are not always available near the high-voltage power lines and space around the poles. On the other hand, mounting recharging stations on power lines is a promising solution because the electromagnetic field around the power cables provides an unlimited power source and the transmission towers do not need to be modified.

Power cable energy harvesting has been studied for numerous applications ranging from transmission system monitoring to electric motor fault detection. Methods for energy harvesting can be divided into two categories: methods based on (i) electric fields and (ii) magnetic fields. In [21], a small tube was installed around a high-voltage cable forming two capacitors connected in series when the transmission conductor and the ground act as two plates. The energy is delivered to the loads in the form of the electric field of the capacitors. The advantage of this method is that the energy harvested does not depend on the amplitude of the power line current. However, the disadvantage of this approach is that it is sensitive to environmental factors such as weather conditions, pollution, humidity, etc. On the other hand, the harvested energy in the form of the magnetic field strongly depends on the current of the power line, but is not affected by environmental conditions. Therefore, this seems to be the more practical method. The structure of this system includes a magnetic core with windings, which can be placed near or clamped around the power cable, and the electronic circuit to convert AC into DC voltage. In [22], a series of experiments was performed with different inductors placed near the power lines in the house. The obtained power was only a few mW, which was not enough to charge the drone's battery, and the inductors were also bulky and heavy. Using a clip-on current transformer is a promising alternative, as it can harvest much more energy while ensuring small and lightweight harvesters. In [23], a coin-sized harvester is succesfully developed that can be clipped around the power cables of electric motors. This provided enough power for a circuit that monitored the vibration of the motors. On the other hand, authors in [24] conducted the same research as [23], but with a larger magnetic core to harvest more energy. Similarly, there have been many other studies to develop sensor nodes that use energy from the magnetic field around power cables instead of batteries [25], [26], [27].

In fact, there is limited work addressing the charging of drone batteries with power line energy. In [28], the authors used the U-shaped inductive core integrated into the drone, which can be firmly attached to the cable with a manipulator. However, the results showed that only 1 W could be harvested from a 1000 A power cable. A more efficient system is proposed in [29], where the authors managed to extract 350 W from a 700 A power line, but the weight of the magnetic core was up to 7.1 kg. Using a high magnetic flux density, Iversen *et al.* [30], [31] developed a very high power density harvester that extracted up to 120 W from an 800 A power line and weighed 1.1 kg (the total mass of the drone is 9.8 kg) based on the theoretical study in [32]. Their system was integrated into a drone and tested on a real power line. It is clear that collecting energy in the form of the magnetic field around power cables is a promising approach, and this method is used for the recharging station in this paper. In addition, although there are studies on magnetic cores, none of them provides a guide for selecting a suitable core and clearly shows the effects of the parameters of each core on the collected energy. Therefore, a detailed guide and analysis of magnetic cores is proposed in this paper.

Although most of the fully developed robotic devices in the literature were intended for power line maintenance, monitoring, or inspection, all applications required the robotic device to be manually attached to the power line [3], [33]. Most of the literature emphasises the installation of the devices and mechanisms using hot sticks [34]. The attaching mechanisms varied from simple linear actuators to complex parallel linkages based on defined design requirements [35]. In [36], an innovative J-type clamp mechanism is presented that works like a wedge system that clamps the electrical wire. The main drawback of the proposed approach is that it still requires manual connection to the power line by an operator. As for the contact between the robot and the power line, the authors in [33] and [37] used a two-point contact principle with a V-shaped slot on the robot side for better grip and larger contact area, which is considered the most promising solution.

Most studies on the development of power line robots do not describe how the featured devices are deployed on the power line or state that they are installed manually [33], [37]. Going a step further in deployment, [38] describes an SDoF aerial manipulator capable of capturing and releasing spherical objects. An SDoF is used because systems with multiple degrees of freedom are heavy and consume more energy. Such a system in the form of a mobile manipulator for the installation and removal of aircraft warning spheres on power lines was successfully developed and tested in [34]. The focus of this study is on aerial robotic installation, i.e., attaching the recharging station to the power line using an aerial manipulator equipped with a special robot end effector.

The contributions of this paper are mainly summarized as follows:

1. The proposed drone recharging station system is designed to be installed with a special SDoF end effector that enables installation with a robotic arm. The end effector enables simultaneous opening/closing of the recharging station and attaching/detaching the recharging station from the end effector. Thus, the recharging station can be easily detached from the end effector when it is closed and firmly attached to the end effector when the recharging station is to be removed from the power line. The proposed design of the recharging station and end effector allows both installation and removal of the recharging station.

2. Since the magnetic core is the most important component of the charging circuits, a detailed analysis of the effects of the core parameters on the harvested power and

load voltage is performed. These parameters are flux density, permeability, number of turns and core shape. In addition, a guideline for the selection of a suitable magnetic core for power harvesting from high current lines is proposed.

3. A prototype of the recharging station electrical system with the main functions has been developed. The proposed electrical system consists of magnetic energy collection, maximum power point tracking (MPPT) and wireless charging. This system has been successfully tested both indoors and outdoors under real grid conditions.

4. The recharging station is equipped with a passive compression spring system that ensures the stability of the recharging station on the power line, i.e. prevents it from tipping over. The recharging station is designed and manufactured from high-strength, low-density materials to be as light as possible.

The rest of the paper is organized as follows. The mechanical design of the recharging station and end effector is presented along with the design requirements in Section II. In Section III, the recharging circuit is presented, focusing on the selection of the magnetic core. Then, in Section IV, the system integration is described, where the mechanical and electrical designs were merged. In addition, experimental results are presented in Section IV to verify and validate the study. Finally, a concluding remark is made in Section V.

II. MECHANICAL DESIGN

In this section, a mechanical design of the recharging station and the robot end effector is presented, from the description of the requirements to the detailed design of the two systems. After explaining the working principle of the system, the focus was on the stability of the recharging station on the power line, the synchronous operation of the mechanisms of the recharging station and the end effector, and the structural integrity of the proposed system.

A. DESIGN REQUIREMENTS

The installation of the recharging station on the power line necessarily requires the mechanical interface between the robotic arm and the recharging station itself. For this purpose, a special robot end effector has been developed to ensure proper attachment of the recharging station to the power line. The main function of the end effector is to attach the recharging station to the power line while ensuring that it can be easily removed from the recharging station once it is installed on the power line. Considering that during the installation of the recharging station, the recharging station must be attached to the power line while the robot end effector detaches from it, it is clear that the proposed system is consisting of the recharging station and the end effector has two separate mechanisms to provide both functions. Since the end effector must transmit power and motion to the recharging station and is mounted on the robotic arm, reducing the degrees of freedom will further reduce the mass and size of the end effector. Therefore, using one SDoF system is a better solution than using two separate SDoF systems to activate

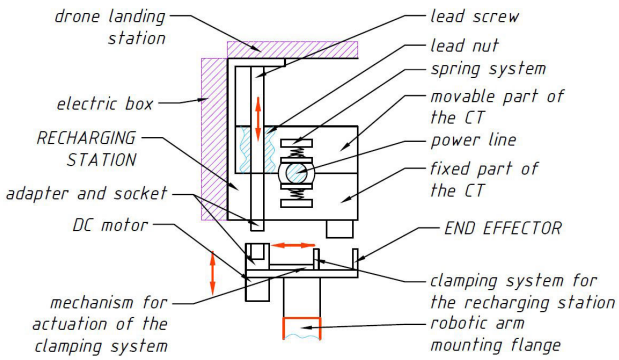

FIGURE 2. Operating principle of the recharging station and robot end effector.

mechanisms. Another limitation arises from the manipulation of such a system with the robotic arm. The entire system must meet certain requirements in terms of mass and size, must not exceed the maximum payload of the robotic arm, and must not make manipulation difficult.

The real environment in which the recharging station is located is highly unpredictable due to the varying weather conditions to which the transmission lines are exposed. Therefore, it is important that the recharging station is firmly attached to the power line. Since the recharging station theoretically only needs to be balanced on a single power line, its stability, i.e., the prevention the overturning of the recharging station, must not be compromised.

Since the drone is charged via the recharging station, the physical interface between the drone and the charging station must be considered, as well as the appropriate way to land the drone at the station. In order to charge the drone, the electrical aspect of the recharging station must also be considered at this stage. Since these two aspects have a major impact on the mass and size requirements, they were considered throughout the design process.

Finally, from the problem described in section I and the derived design requirements, the final configuration of the proposed system must fulfil the following functions:

1. Being as light and compact as possible without violating the structural requirements,

2. Attaching of the recharging station to the power line and simultaneously removing the end effector from it by using an SDoF system and vice versa,

3. Connecting the two ferromagnetic parts of the recharging station to each other,

4. Ensuring the stability of the recharging station on the power line, i.e. preventing the overturning on the recharging station on the power line,

5. Securing a docking station for the drone and the space for the electronics of the recharging station.

B. OPERATING PRINCIPLE OF THE RECHARGING STATION AND THE END EFFECTOR

Based on the requirements, the functional principle of the recharging station and the end effector is defined. The

split-core current transformer (CT) is used to harvest energy from the power line. It consists of two ferromagnetic cores arranged in the movable and fixed parts of the CT, respectively. In order to harvest energy, the two cores must be in contact. The movable part of the CT is actuated by the lead screw-nut mechanism, which is driven by the DC motor on the end effector (see Figure 2). The same motor actuates the clamping system on the end effector, which is responsible for fastening and releasing the recharging station. In the pre-installation position, the end effector is mounted on the mounting flange of the robotic arm and the recharging station is placed and secured on the end effector. The recharging station is open, i.e. the two ferromagnetic cores are not touching. In this way, the recharging station can be attached to the power line using the robotic arm and the end effector. Once it is placed around the power line, the motor starts to rotate. The rotation of the motor sets two mechanisms in motion simultaneously: (i) the lead screw mechanism and (b) the clamping system mechanism. Geometric considerations of the recharging station and the end effector must be taken into account to ensure synchronous operation of the mechanisms. The lead screw mechanism activates the linear movement of the movable part of the CT, and the clamping system mechanism starts to release the recharging station from the end effector. When two ferromagnetic cores touch each other, the recharging station is fully released and the robotic arm can move together with the end effector from the recharging station. At the same time, the stability of the recharging station, i.e. preventing it from tipping over since the center of mass (CoM) of the recharging station is not in the middle of the power line, is ensured by the spring system. The spring system compresses during the installation phase, ensuring stability on the power line.

Figure 2 represents the proposed recharging station and the end effector. The system has a single-degree-of-freedom that ensures the closing/opening of the ferromagnetic cores inside the current transformer, as well as the attachment and removal of the end effector to and from the recharging station. The closing of the recharging station is enabled by a lead screw mechanism. The spring system ensures that the recharging station is firmly attached to the power line. The figure also shows the designated places for the electronics box and the landing station of the drone (purple dashed lines).

C. RECHARGING STATION STABILITY ON POWER LINE

The attaching of the recharging station to the power line means that the two ferromagnetic core parts are connected and that the recharging station is not overturning on the power line. The stability condition tends to deteriorate due to the action of the moments caused by the forces shown in Figure 3. Therefore, the stability condition of the recharging station is:

$$\sum_i \vec{M}_{C_i} = \vec{0}; \tag{1}$$

$$\begin{aligned} 2F_{fr}r - G_{\text{all}}x_{CS} - G_{\text{el.box}}x_{\text{el.box}} \\ + (G_{\text{dock}} + G_{\text{drone}})x_{\text{drone}} = 0, \end{aligned} \tag{2}$$

where F_{fr} is the frictional force that occurs in contact between the power line and the recharging station, $r = d/2$ the radius of the power line, G_{all} the total weight of the recharging station without electronic box and docking station assembly, x_{CS} the shortest distance from the CoM(CS) of the recharging station to the point C (the center of the power line, i.e. the electric wire), $G_{\text{el.box}}$ the total mass of the electronic box assembly, $x_{\text{el.box}}$ the shortest distance from the CoM of the electronic box assembly to the point C, G_{dock} the total weight of the docking station, G_{drone} the total weight of the drone that will be charged from the recharging station and x_{drone} the shortest distance from the CoM of the docking station to the point C.

The compression spring system is added to ensure the stability of the recharging station on the power line. It consists of four compression springs divided into two springs in series and two in parallel. The compression springs are preloaded in the opening position. When the two ferromagnetic parts of the current transformer (CT) are closed by operating of the trapezoidal drive shaft, the springs are compressed more, exerting the normal force on the electric wire, i.e. the power line. The resulting forces in the springs cancel out the bending moments that seek to destabilize the overall system during assembly and/or operation by ensuring significant frictional force moment on the power line.

The frictional force needed to prevent the overturning of the recharging station is generated by the normal force that occurs when the springs are compressed. The closing sequence is implemented so that at the point where two ferromagnetic parts touch, the force that arises in the compression springs is sufficient to hold the recharging station on the power line by friction. But to ensure the function of the compression springs, i.e. the constant factor of the compression spring c must be chosen properly.

The frictional force from Equation (2) according to the Coulomb's Law of Friction is:

$$F_{fr} = \mu F_N, \tag{3}$$

where in this case the normal force F_N, because of the disposition of the compression springs (see Figure 3) is equal to:

$$F_N = F_{S2} = \frac{F_S}{2}, \tag{4}$$

where μ is the coefficient of the friction between the power line (steel) and the contact surface on the recharging station, F_{S2} is the combined force of two compression springs in series and F_S is the force that occurs in the compression spring thus ensuring the stability of the recharging station on the power line.

The elasticity of the compression spring, assuming that the spring will behave exclusively linear-elastic, is defined as:

$$F_S = c\Delta z = c(z_2 - z_1), \tag{5}$$

where the c is the constant factor of the compression spring and Δz is the difference of the initial and ending position of

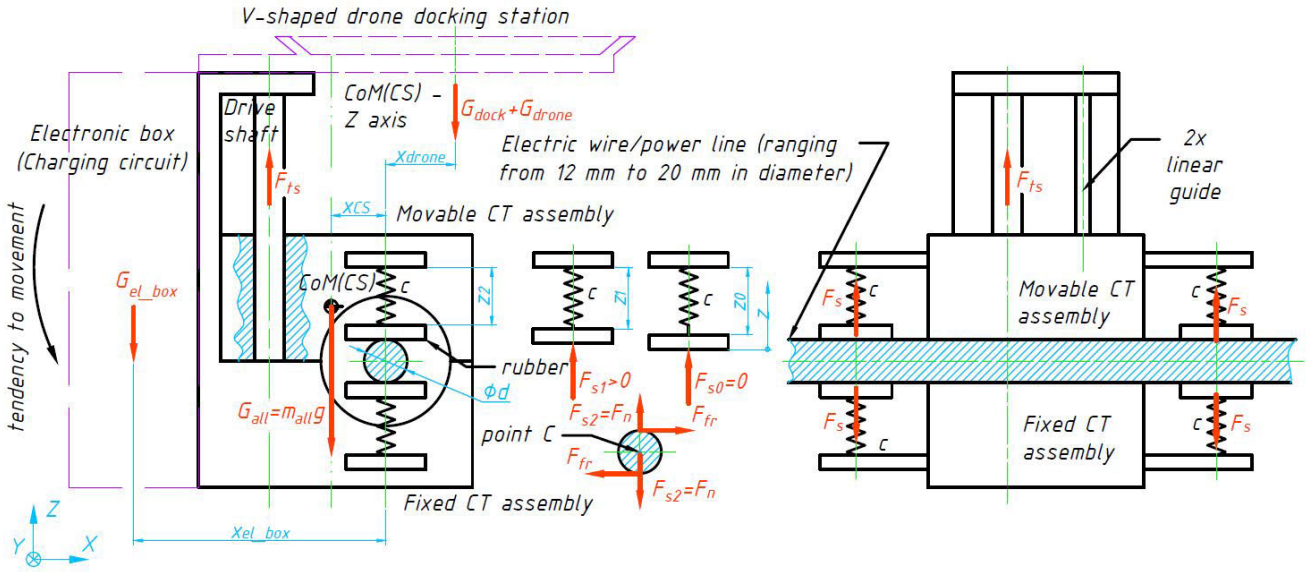

FIGURE 3. Simplified schematic of a small drone recharging station mounted on a power line.

the spring. The normal force that occurs in the compression spring and holds the recharging station firmly on the power line is:

$$F_S = \begin{cases} F_{S-\text{wdrone}} & \text{with the drone,} \\ F_{S-\text{wodrone}} & \text{without the drone.} \end{cases} \tag{6}$$

Now the Equation (5) can be written as:

$$c_{min} = \frac{max(F_S)}{\Delta z}. \tag{7}$$

The selected constant factor must be (a) greater than the minimum constant factor and (b) chosen to increase the reliability and safety of the recharging station on the power line, given the environment and conditions for installation and drone landing. Therefore, the safety factor for stability can be calculated as follows:

$$S = \frac{c}{c_{min}}. \tag{8}$$

To mitigate the swing effect at the recharging station due to environmental conditions (wind, ice, etc.), the safety factor given in Equation (8) should be between 2 and 5. In this way, the connection between the recharging station and the power line will be more stable and reliable.

D. SYNCHRONOUS OPERATION OF MECHANISMS

Since the reduction of the degrees of freedom helps to reduce the mass and the size of the whole system, it is necessary to operate both mechanisms simultaneously in order to attach the recharging station to the power line and detach the end effector from it at the same moment and vice versa.

The end effector and the recharging station are in three-point contact: two points (two clamp extensions) for holding the recharging station to ensure stability and a firm grip, and one point (pyramid-shaped shaft adapter) for transmitting power from the end effector to the trapezoidal drive shaft of the recharging station.

An SDoF system (DC motor) is used to move both mechanisms. Nevertheless, the system geometry must be taken into account to ensure the simultaneous operation of the mechanism. The attaching of the recharging station to the power line is made possible by the work of the trapezoidal drive shaft, which results in a translational motion of the movable part of the current transformer to the fixed part of the current transformer. Although the input to the trapezoidal drive shaft is the rotational motion, the translational motion is provided by the addition of two linear guides that prevent rotation of the movable part of the current transformer. To detach from the recharging station, i.e. to attach to it, the clamping extensions are added. On the side of the end effector there is the subsystem for clamping or unclamping, which is enabled by the wedge system. The wedge system also moves translationally and ensures that the recharging station is clamped to the end effector and vice versa. During the release sequence, the spring system pulls the wedge system back from the clamp extensions and releases the recharging station (see Figure 4).

From the DC motor the power is supplied to the recharging station, moving the movable part of the current transformer to the fixed part and to the clamping subsystem by means of timing pulleys and belt. On the driven pulley side, the middle part of the driven shaft is threaded to ensure the translational motion of the drive wedge. The shape of the wedges prevents rotation and thus secures the clamping.

The number of revolutions of the trapezoidal drive shaft required to close the two parts of the ferromagnetic core can be calculated as follows:

$$n_{t1} = \frac{z_1}{P_1}, \tag{9}$$

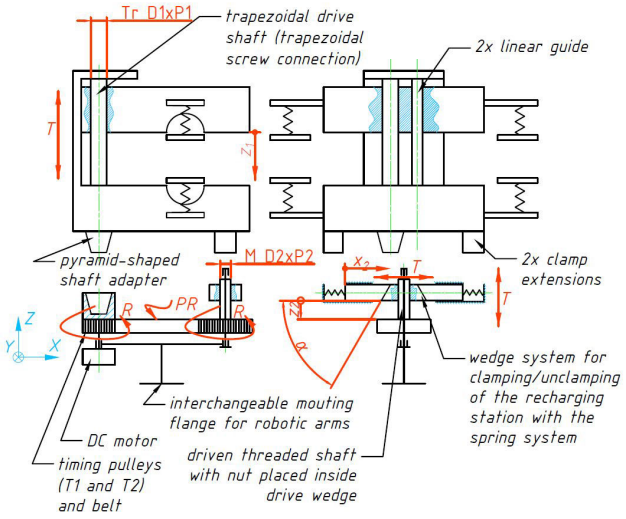

FIGURE 4. **Mechanical principle of simultaneous operation of the mechanism driven by a DC servo motor (R - rotational movement; T - translational movement; D1, D2 - nominal thread diameter; P1, P2 - thread pitch; *PR* - pulley ratio).**

where z_1 is the distance required to ensure attachment of the split-core ferromagnetic parts, and attachment of the recharging station to the power line, and P_1 is the trapezoidal drive shaft pitch.

Similarly, the distance required to detach from or attach to the recharging station is defined as x_2. Considering that the wedges interact with each other, the distance that must be traveled on the driven threaded shaft is:

$$z_2 = n_{w2} P_2 = \tan\alpha x_2, \tag{10}$$

where n_{w2} is the number of revolutions of the driven threaded shaft, P_2 is the pitch of the driven threaded shaft, and α is the angle between the driving and driven wedges. Since the two aforementioned mechanisms are connected by a belt drive, the pulley ratio is calculated as follows:

$$PR = \frac{z_{p2}}{z_{p1}}, \tag{11}$$

where z_{p2} and z_{p1} are the number of teeth of the driven and the driving pulley, respectively.

By combining equations (9), (10) and (11), the pitch of the driven threaded shaft pitch can be calculated from the following expression:

$$P_2 = \frac{z_2 PR}{n_{t1}}. \tag{12}$$

Finally, the simultaneous work of the mechanism will only be achieved if both of threaded shafts are right-handed or left-handed. As shown in Figure 4, opening and closing of the recharging station is provided by the work of the trapezoidal drive shaft. On the end effector side, the release from, and attachment to the recharging station is performed by the wedge system. Both mechanisms work simultaneously using the timing pulley system in combination with the drive threaded shafts, ensuring both actions.

E. STRUCTURAL ANALYSIS OF THE MECHANISM

After the working principle is established, it is important to determine the effect of loads on physical structures, i.e. the structural integrity of the system. The trapezoidal drive shaft is the vital part of the recharging station and in combination with a trapezoidal nut it attaches the recharging station to the power line and provides the physical contact between two ferromagnetic parts. Therefore, the maximum force that occurs on the trapezoidal drive shaft in the direction of Z axis, according to the Figure 3, is:

$$F_{ts} = 2F_S + G_{\text{movCT}} + F_{\text{core}}, \tag{13}$$

where G_{movCT} is the weight of the movable part of the current transformer assembly, i.e. the part that moves together as the trapezoidal drive shaft rotates, F_{core} is the force needed to attach two ferromagnetic parts of the core which was defined experimentally during the design process. The torque needed to provide F_{ts} force in the trapezoidal drive shaft can be calculated as:

$$T_{ts} = F_{ts}\frac{d_2}{2}\tan(\alpha + \rho'), \tag{14}$$

where d_2, α and ρ' depend on the type of the trapezoidal thread and the material selection of the lead nut and screw. This particular trapezoidal thread is self-locking ($\alpha < \rho'$) which means that the lead nut or lead screw cannot be moved without the external force.

The torque on the DC motor required for trapezoidal drive shaft is:

$$T_{\text{EM}ts} = \frac{T_{ts}}{\eta_{ts}\eta_{\text{EM}}}, \tag{15}$$

where the η_{ts} is the efficiency of the trapezoidal screw that depends on α and ρ', and η_{EM} is the efficiency of the DC servo motor. As the torque requirement for operating the wedge system mechanism is negligible compared to the torque requirement for driving the trapezoidal drive shaft, the overall torque on the DC motor is:

$$T_{\text{EM}} \geq T_{\text{EM}ts}. \tag{16}$$

F. DETAILED TECHNICAL DESIGN OF THE SYSTEM

The final design of the recharging station with its end effector for attaching it to the power line is shown in Figure 5. The Dynamixel MX-64 DC motor placed on the end effector transmits power and motion to the trapezoidal drive shaft on the recharging station and to the threaded M10 × 0.75 steel shaft on the end effector through the timing belt. For the trapezoidal drive shaft the trapezoidal thread Tr12 × 3 made of steel C45 is chosen along with the brass lead nut to minimize the pressure velocity parameter. The combination of the above mentioned shafts, i.e. screws, ensures the synchronous operation and structural integrity of mechanisms described in II-D and II-E.

As the robot end effector after the installation of the recharging station will move from it, the adapter on the recharging station is pyramid-shaped so that the end effector

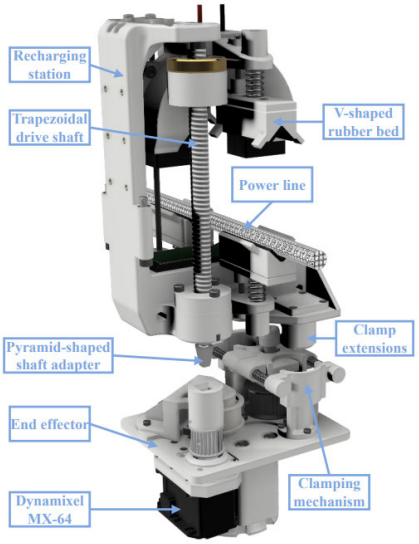

FIGURE 5. The detailed design of the recharging station and the end effector shown in virtual CAD environment.

TABLE 1. Final design parameters of the recharging station and the robot end effector to meet all the requirements.

c	8.25 N/mm
Δz_{max}	10 mm
z_{p1}	24
z_{p2}	34
P_1	3 mm
P_2	0.75 mm
z_1	63 mm
x_2 (z_2)	11 mm
α	45°

can move freely to and from it when needed without difficulties. The lead nut is prevented from rotation by two linear guides, since it is placed rigidly on the movable part of the current transformer. The contact area between the power line and the recharging station is improved in terms of having more contact points. The rubber on the recharging station is in V-shaped bed ensuring contact in two points making the whole system more reliable. The driven wedge is designed to hold the recharging station once the clamping subsystem is active ensuring that the clamp extensions are inside the end effector.

Finally, to ensure the proper work of the recharging station and the robot end effector described in previous subsections, the final design consists of elements presented in Table 1, considering the limitations coming from the manufacturing standards and techniques.

III. ELECTRICAL DESIGN

In this section, the electrical system of the recharging station is presented. Figure 6 shows how the electrical components of the recharging station and the drone are connected. The split-core with windings is used to harvest energy from the magnetic field of the power line. The rectifier converts the voltage from AC to DC. The MPPT circuit is used

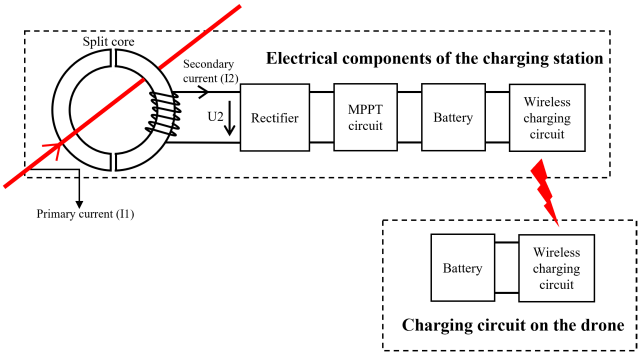

FIGURE 6. The electrical system of the recharging station and the drone.

to charge an auxiliary battery of the recharging station, which acts as a buffer to ensure constant charging power for the drone as the energy drawn from the power cable fluctuates greatly. When the drone lands on the recharging station, it is charged wirelessly. Since the power line is the main energy source, the most important part of the recharging station is the magnetic core, so the main focus is on it. In addition, the operating conditions in Table 2 should be considered when designing the electrical system.

TABLE 2. Operating conditions of the recharging station.

Condition	Unit	Value
Power line voltage	kV	15
Operating frequency	Hz	50 ÷ 60
Power line diameter	mm	20 ÷ 45
Range of power line current	A	200 ÷ 1000

A. MODELLING ENERGY HARVESTING UNIT

The magnetic core contains many parameters such as flux density, permeability, air gaps, dimensions, shapes, etc. To select a suitable core for a particular application, it is necessary to analyze the effects of these parameters on the harvested power. Simulation is a viable approach for quick analysis instead of performing many experiments. The voltage transformer model was proposed in [39], so the current transformer model based on [39] is established to estimate the power harvested from cables. According to Ampere's law, the following holds:

$$n_1 i_1 + n_2 i_2 = H l_m, \tag{17}$$

where n_1 and n_2 are the number of turns of the primary and secondary windings (n_1 is equal to 1 in this case), i_1 and i_2 are primary and secondary currents, H is the magnetic intensity, and l_m is the magnetic length of the core (Figure 7).

Since $H = B/\mu$ and $B = \phi/Ac$, the F can be expressed as:

$$F = H l_m = \frac{l}{\mu A_c}\phi = \Re\phi, \tag{18}$$

where $\Re$ is the core's reluctance, μ is permeability, ϕ is magnetic flux, B is flux density and A_c is the cross-sectional area of the core.

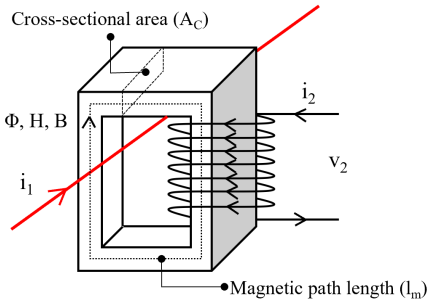

FIGURE 7. The model of a magnetic core.

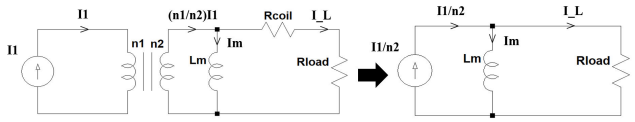

FIGURE 8. Equivalent circuits of the magnetic core.

According to Faraday's law, the following applies:

$$v_2 = n_2 \frac{d\phi}{dt}. \tag{19}$$

Including Equation (17) to (19) gives:

$$v_2 = \frac{{n_2}^2}{\Re} \frac{d(\frac{n_1}{n_2} i_1 + i_2)}{dt} = L_m d \frac{i_m}{dt}. \tag{20}$$

Based on Equation (20), the magnetizing inductance L_m and magnetizing current i_m (Figure 8) are calculated by Equations (21) and (22) as follows:

$$L_m = \frac{{n_2}^2}{\Re} = \frac{{n_2}^2 \mu A_c}{l_m}, \tag{21}$$

$$i_m = \frac{n_1}{n_2} i_1 + i_2. \tag{22}$$

The magnetizing current i_m is proportional to the flux density B in the core. A large value of i_m leads to saturation of the core. The saturation depends on both i_1 and i_2, not only on each of them.

From Equations (17) and (22), the relationship between the magnetizing current i_m and flux density B is shown in Equation (23).

$$B = \frac{n_2 i_m \mu}{l_m}. \tag{23}$$

Figure 8 (left) illustrates the equivalent circuit of the harvesting system. The secondary current i_2 is calculated by the Equation (24), where the number of turns of the primary side is $n_1 = 1$.

$$i_2 = i_1 \frac{n_1}{n_2} = \frac{i_1}{n_2}. \tag{24}$$

The resistance of the secondary winding R_{coil} can be neglected when calculating the load voltage because it is very small compared to the load resistance R_{load}, but it is still useful for estimating the power loss. Therefore, the equivalent circuit can be simplified to the circuit in Figure 8 (right). The voltage of the load is given by Equation (25), where $\omega = 2\pi f$, f is the frequency of the power line AC (50 Hz in this case).

$$U_{\text{load}} = \frac{i_1}{n_2} \frac{\omega L_m R_{\text{load}}}{\sqrt{\omega^2 {L_m}^2 + {R_{\text{load}}}^2}}, \tag{25}$$

$$P_{\text{beforeLoss}} = \frac{{U_{\text{load}}}^2}{R_{\text{load}}}. \tag{26}$$

The power consumption of the load is calculated by Equation (26). In order to get maximum power from the AC power line, R_{load} must be set to a suitable value, as shown in Figure 9 (left, blue line). This value must correspond to the impedance of the magnetizing inductor L_m. In other words, the maximum load power can be achieved only when R_{load} is equal to $Z_{L_m} = \omega L_m$ (resistive matching). It is possible to get much higher power with impedance matching circuits using capacitors, but this is not necessary because of the saturation of the magnetic core. The maximum harvested power in Figure 9 (left) applies only to the ideal core, which never get saturated. It can be seen that the maximum power is reached at a flux density of about 7 T (see Figure 9 - left, red line). Currently, the material with the highest flux density (cobalt-iron) is only 2.4 T, so the maximum power that can be harvested from the power line is limited by the saturation of the core. Very little power can be harvested within the saturation range because the permeability of the core is close to the permeability of air. Instead of manually adjusting the load, the MPPT circuit automatically finds the point of maximum power (before the saturation point). Figure 9 (right) shows the large difference between the power harvested from the ideal and the saturation core.

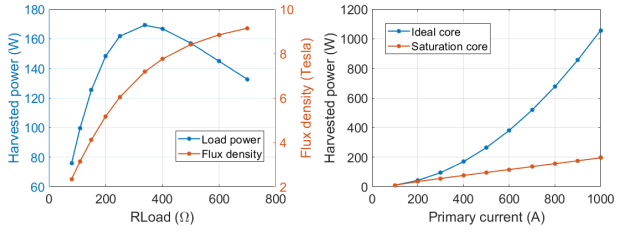

FIGURE 9. Harvested power of an ideal core and a saturation core.

There are two main types of losses of the magnetic core: (i) winding losses (caused by coil resistance) and (ii) core losses (caused by eddy current). Equation (27) shows how to calculate the winding loss P_{Cu}:

$$P_{Cu} = {I_L}^2 R_{\text{coil}}, \tag{27}$$

where I_L is the load current and R_{coil} is the resistance of the windings. Also, Equation (28) shows how to calculate the core loss P_{Fe}:

$$P_{Fe} = WK \cdot m_{Fe}, \tag{28}$$

where WK is the power loss per kilogram (W/kg). This parameter is usually given in the core datasheet, and m_{Fe} is

the mass of the core. Finally, the harvested power is:

$$P_{\text{afterLoss}} = P_{\text{beforeLoss}} - P_{Cu} - P_{Fe}. \tag{29}$$

In [39], the increasing temperature (T_r) caused by power losses is estimated by Equation (30). This information is important when selecting the core material and wire size of the windings to ensure that the core temperature is below an acceptable value.

$$T_r = 450 \left(\frac{P_{Cu} + P_{Fe}}{A_t} \right)^{0.826}, \tag{30}$$

where A_t is the surface area of the core.

B. ANALYZING CORE PARAMETERS

In this subsection, the relationship between the core parameters and maximum harvested power is analyzed. Core selection guidelines are proposed to select the most suitable magnetic core for the power line application.

1) FLUX DENSITY

The saturation flux density (B) is an important characteristic of a magnetic core. As mentioned in part III-A, the ideal core can harvest much more energy than the saturation core because the flux density never get saturated (see Figure 9 - right). Therefore, it makes the most sense to use the core material with the highest saturation flux density. Different core materials have different values of saturation flux density. Table 3 shows the information about some common magnetic materials. It can be seen that cobalt-iron (Co-Fe) has the highest magnetic saturation, up to 2.4 T. Other common materials such as ferrite have low magnetic saturation but high resistivity (low eddy current). Therefore, the low core loss is the main reason why ferrite is normally used in high frequency circuits. At low frequencies (50 Hz), high magnetic flux materials such as cobalt-iron and silicon steel have lower resistivity than ferrite, but the harvested power is still much higher than the power loss (about 1.5 W at 1.9 T and 50 Hz with silicon steel). So the best option is to use the core material with the highest saturation flux density.

2) PERMEABILITY

Permeability is a parameter that indicates how well a magnetic material can conduct flux. The higher the value of permeability, the better the ability to conduct flux. This parameter is defined as the ratio of magnetic flux B to magnetic intensity H - see Equation (31). H is proportional to the sum of the primary and secondary currents according to Ampere's law described in Equation (17).

$$B = \mu H = \mu_0 \mu_r H, \tag{31}$$

where $\mu_0 = 4\pi 10^{-7} \frac{\text{H}}{\text{m}}$ is the permeability of air, μ_r is the relative permeability of the magnetic core, and μ is the absolute permeability. However, in the case of the split core, the air gaps between two halves significantly affect the relative permeability of the core μ_r. The effective permeability of the core with air gaps (μ_e) can be calculated by Equation (32), where l_g is the length of the air gaps. Currently, cores with very small air gaps (0.01 mm ÷ 0.03 mm) can be manufactured to maintain the relative permeability [43], [44].

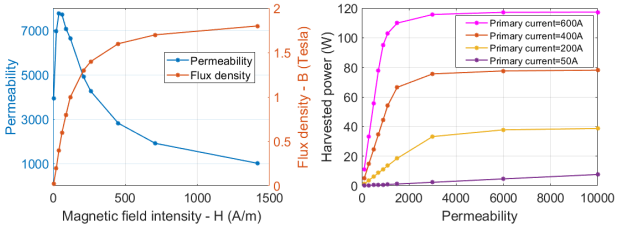

FIGURE 10. *B – H* graph (left) and permeability vs. harvested power (right).

$$\mu_e = \frac{\mu_r}{1 + \mu_r \left(\frac{l_g}{l_m} \right)}. \tag{32}$$

As can be seen in the $B - H$ graph (Figure 10 - left), the permeability of the core is not constant. In fact, it drops rapidly to as low as 1000 when B is 1.8 T. As H is further increased, the flux density B gradually gets saturated when the permeability of the core is close to the permeability of air. The flux will alternate slightly in this region, and a little energy can be harvested. However, the use of a magnetic core with very high permeability is not always necessary. In Figure 10 (right), the relationship between permeability and maximum harvested power is simulated in different cases of primary current (from 50 A to 600 A). When the power line current is greater than 200 A, permeability has almost no effect on the harvested power when μ is greater than 2000. In other words, the harvested power becomes saturated. For example, since the recharging station is installed on a high current power line ($\geq$ 200 A), nanocrystalline with the highest permeability in Table 3 should not be chosen. Instead, silicon steel with moderate permeability (above 2000) and high flux density is a wiser choice. Air gaps should be considered when calculating the permeability of a split core. In addition, this feature can be used to simplify the model since most common magnetic materials have an average permeability greater than 2000. Instead of creating a complex function to model the nonlinear relationship between μ and H (Figure 10 - left), it is possible to use a constant value ($\geq$2000) of μ when simulating at a high power line current.

However, if the primary current is less than 50 A, a core with higher permeability may be a better choice. In this case, the harvested power is still proportional to the permeability (Figure 10 - right) because the saturation point is somewhere beyond the graph when μ is greater than 10000. To prove this, two different cores operated on a 20 A power line are considered by simulation (see Table 4). It can be seen that the core with a high magnitude of permeability harvests more power than the other with a high magnetic flux.

TABLE 3. Parameters of some common magnetic materials, unit price for a core of about 700 g.

Material	Magnetic saturation (T)	Permeability	Resistivity (Ωcm)	Unit price (EUR)	References
Supermendur (Co-Fe)	1.9 ÷ 2.4	800 ÷ 19k	$40 \times 10^{-6} \div 44 \times 10^{-6}$	630 ÷ 2300	[39]–[42]
Silicon Steel (Si-Fe)	1.5 ÷ 2.1	2k ÷ 52k	$40 \times 10^{-6} \div 47 \times 10^{-6}$	80 ÷ 220	[39], [41]–[44]
Ferrite (Mn-Zn)	0.3 ÷ 0.5	750 ÷ 15k	10 ÷ 100	15 ÷ 50	[39]
Nanocrystalline (Fe-Cu-Si-Nb-B)	1.0 ÷ 1.2	30k ÷ 200k	115×10^{-6}	15 ÷ 50	[39], [41], [42]

TABLE 4. Harvested power of two cores with the same weight and different permeability when the primary current is 20 A.

Core	Magnetic saturation (T)	Permeability	Harvested power (W)
Core 1	1.2	10^5	2.0
Core 2	2.1	10^4	1.2

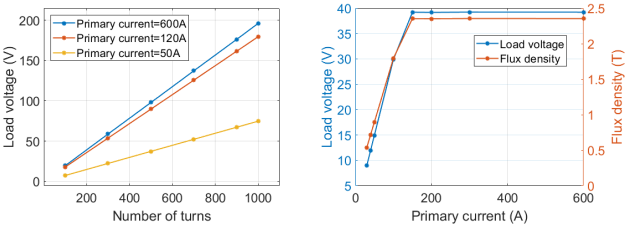

FIGURE 11. Number of turns vs. load voltage (left) and current vs. load voltage, flux density (right).

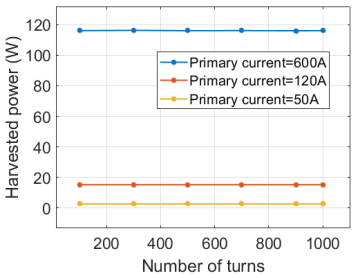

FIGURE 12. Number of turns vs. harvested power.

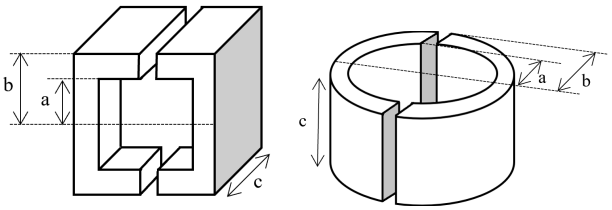

FIGURE 13. C-core (left) and Toroidal core (right).

3) NUMBER OF TURNS

A simulation was conducted to show the relationship between the number of wire turns and the load voltage at the point of maximum power. As shown in Figure 11 (left), it can be seen that the larger the number of turns, the higher the load voltage. Moreover, in Figure 11 (right) the higher the primary current, the higher the load voltage, but this is true only when the primary current is low. More precisely, the load voltage (blue line) is proportional to the power line current until it is stable at about 39 V. The reason for this is that when the current is low (under 150 A in this case), maximum power can be harvested if the magnetic core is not near saturation region, as shown in Figure 11 (right, red line). When the current is greater than 150 A, the highest power can always be reached just before the core gets saturated, so the load voltage is now constant. In addition, in Figure 12, the number of wire turns does not affect the maximum harvested power. Therefore, a high number of turns (high load voltage) results in a low charging current and vice versa. The number of turns should be determined considering the battery voltage of the recharging station and the MPPT circuit. Power loss and temperature rise should also be considered when selecting the wire size and number of turns. If the same wire size is used, the core with the higher number of turns (high voltage, low current) will have less winding loss and temperature rise than the other with low turns (low voltage, high current). However, more wire turns means that the core is heavier.

4) CORE SHAPE

In this part, the performances of two different core forms are presented and compared: C-core and toroidal core (Figure 13). For the same inner radius a, outer radius b, and height c, the toroidal core has a smaller magnetic path length (l_m) than the C-core, but the same cross-sectional area (A_c). Therefore, a toroidal core will harvest more energy than a C-core. Also, the toroidal core is lighter than a C-core with the same dimensions a, b, and c. However, the surface area of toroidal core is smaller than that of the C-core, so the heat dissipation performance of toroidal core will be worse than that of the C-core. Therefore, a larger wire diameter should be used for the toroidal core to reduce the power loss.

Figure 14 (left) shows the results of a simulation with different core masses (both core and windings) to compare the maximum harvested power of C-core and toroidal core. The core mass is increased by changing the height c to keep the magnetic path length (l_m) unchanged but increase the cross-sectional area (A_c). C-core with a wire diameter of 0.7 mm is used, and the diameter of the toroidal core wire is 0.9 mm. The test was simulated with a primary current of 600 A. As can be seen that with the same harvested

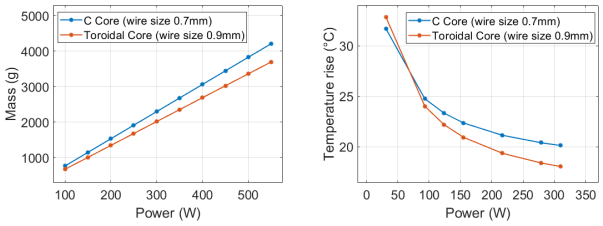

FIGURE 14. Mass vs. harvested power (left) and temperature rise (right) of C-core and toroidal core.

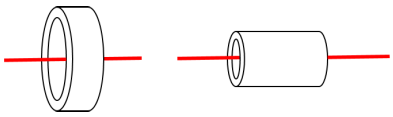

FIGURE 15. Short core (left) and long core (right).

power, the toroidal core is much lighter than the C-core. In other words, the toroidal core has a higher power density (W/g) than the C-core. For example, to harvest 150 W, about 150g can be saved if the toroidal core is used instead of a C-core. Furthermore, in Figure 14 (right) shows that a toroidal core with a wire diameter of 0.9 mm also has better thermal performance than a C-core.

As discussed above, the length of the magnetic path (l_m) and the cross-sectional area (A_c) have a strong influence on the harvested power if a core with short l_m and large A_c is to be chosen. Therefore, selecting a long core with small diameter (Figure 15 - right) is better than selecting a short core with large diameter (Figure 15 - left). For the same mass, the long core has a shorter l_m and a wider A_c than the short core, so more power can be extracted from the power line when using the long core. In fact, the short magnetic path length (l_m) reduces the permeability according to Equation (32), and the long core has heavier windings than the short core. However, the advantages of the long core outweigh the disadvantages. Table 5 and Figure 16 compare the performance of two cores with the same mass (core and windings) and the temperature rise. When using the long core instead of the short core, an additional power of 43% up to 70% can be harvested.

C. MAGNETIC CORE SELECTION GUIDELINE

The magnetic core is selected according to the following criteria, which ensure a lightweight system and meet the operating conditions in Table 2:

1. The flux density of the core should be as high as possible,
2. Permeability: not necessary be very high, but should be greater than 2000 (with air gaps),
3. Number of turns: consider the input voltage of the MPPT circuit and the battery voltage of the recharging station,
4. Core shape: round and long shape, the specific dimensions should be determined taking into account the desired charging time and the total weight of the recharging station.

Table 3 shows four common magnetic materials on the market. The core material with the highest magnetic saturation is Supermendur (Co-Fe), but the price for a 700 g core is

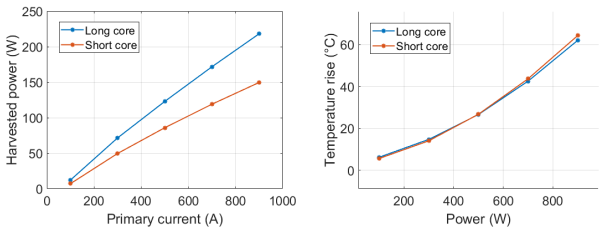

FIGURE 16. Harvested power (left) and temperature rise (right) of the long and short cores.

TABLE 5. Parameters of the long and short cores.

Parameter	Unit	Short core	Long core
Core material	-	CoFe	CoFe
Relative permeability	-	6000	6000
Effective permeability (air gaps 0.05 mm)	-	2666	2087
Inner diameter	mm	50	30
Outer diameter	mm	70	50
Height	mm	37.5	51.6
Magnetic path length (l_m)	mm	240	160
Cross sectional-area (A_c)	mm^2	375	516
Core mass	g	731	670
Winding mass	g	56	117
Total mass	g	787	787

very expensive (up to 2300 EUR). Due to its low resistivity, ferrite has the lowest core loss, but the magnetic flux density is also very low. Nanocrystalline is cheap and has a very high permeability, but the magnetic saturation is quite low. Finally, silicon steel (Si-Fe) is the best option because it is inexpensive, has high magnetic density and relatively high permeability.

D. ELECTRICAL COMPONENTS OF THE RECHARGING STATION

Based on the selection guideline from III-C and the operating conditions in Table 2, the toroidal core from Hobut [44] is selected for the recharging station. It is made of silicon steel (Si-Fe) with a maximum permeability of 7876. The detailed parameters of this core are the same as those of core 2 in Table 6 of the experimental part (IV-B) except for the number of turns. Since the LiPo 4S 1800 mAh battery is used, the number of turns is 185. The load voltage at maximum power is about 20 V ÷ 21 V. Since the output voltage of the magnetic core is AC, a rectifier is used to change the voltage from AC to DC. The MPPT circuit will track the point of maximum power to charge the battery automatically (Figure 6). Figure 17 illustrates the relationship between the load voltage and the harvested power. It can be seen that maximum power can always be achieved at a certain load voltage (33 VDC in the simulation case), but this is only true if the primary current is high enough, as discussed in III-B2. Thus, a simple method to locate the point of maximum power

is to regulate the load voltage (the input voltage of the MPPT circuit) to an appropriate level. This feature of magnetic cores is very similar to that of solar cells, so a large number of IC controllers can be used for the recharging station. The BQ24650 IC controller from Texas Instruments is not only able to regulate the input voltage, but also to monitor and charge different types of batteries.

There are two methods to charge drones when they land on the station: (i) wired charging and (ii) wireless charging. Since the recharging station is operated outdoors, the wired charging method is not practical. The connector contact surface may wear out over time and is exposed to dust and water, requiring regular cleaning. In contrast, wireless charging is a better solution because the receiving and transmitting coils can be housed in enclosures and still function properly. Commercially available wireless charging circuits with a maximum charging power of 36 W are used for the recharging station. The charging power is influenced by a number of factors, such as the input voltage of the transmitter, the distance and position between the charging coils, etc.

IV. EXPERIMENTAL VALIDATION AND RESULTS

In this section, the proposed recharging station and the robot end effector are integrated, tested and validated under laboratory conditions and in a real power line environment. Following experiments were conducted: a) robotic installation and removal of the recharging station to and from the power line using a robotic arm, b) the validation of the charging circuit both indoors and outdoors, and c) the validation of charging process in the real power line environment of the fully integrated recharging station.

A. RECHARGING STATION INSTALLATION

In this subsection, the laboratory experiments for robotic installation and removal of the recharging station are presented. For this experiment, the SCHUNK LWA 4P 6DoF robot arm (SCHUNK robot arm) with a fixed base is used to verify and validate the desired mechanical behaviour of the mutual physical interface between the end effector and the recharging station. In addition, a power line is stretched through two fixed towers representing the real environment. For this purpose, the SCHUNK robot arm and the Dynamixel MX-64 DC motor on the end effector are controlled and driven via the ROS interface. Figure 18 shows the installation procedure of the recharging station on the power line in three steps (left, centre and right). *Left*: the system is in the pre-installation phase with the recharging station open and attached to the robot end effector. *Centre*: the recharging station begins to close and connect to the power line while simultaneously detaching from the robot end effector. *Right*: the recharging station is attached to the power line and is prevented from tipping over. The robot end effector and robotic arm are moved away from the recharging station.

The first experiment (I) consists of two parts: (i) attaching the recharging station to the power line using the robotic arm while removing the end effector from it, and detaching

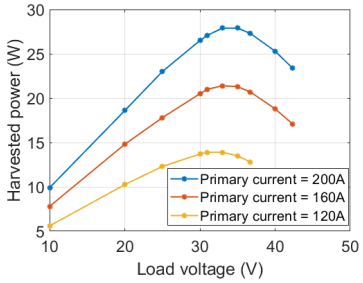

FIGURE 17. Load voltage vs. harvested power.

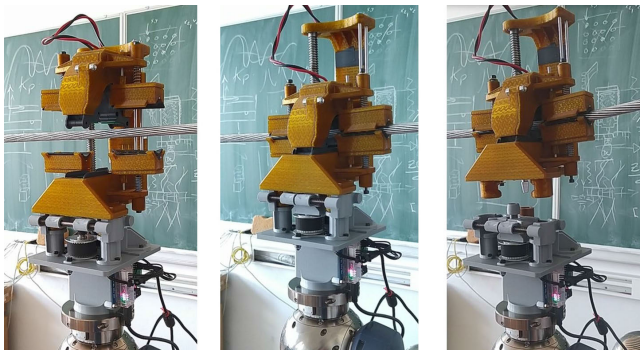

FIGURE 18. Installation procedure of the recharging station on the power line in three steps (left, centre and right).

the recharging station from the power line using the robotic arm while ensuring a firm connection between the recharging station and the end effector, and (ii) measuring in time of two physical quantities via the ROS interface: the Dynamixel MX-64 DC motor current and the angular position of the DC motor flange. In the second experiment (II) the maximal force that occurs in the trapezoidal drive shaft when attaching the recharging station to the power line was measured along with the Dynamixel MX-64 DC motor current and the angular position of the DC motor. The force was measured using the 6-axis OptoForce force and torque sensor. In experiment (I), both motor current and position are measured during the installation and removal of the recharging station. Since it was not possible to measure the above force during experiment (I), the force measurement was performed separately from the power line along with the current measurement to validate the experiment (II). As seen in the graph (see Figure 19), the DC motor current suddenly rises in the beginning of the installation due to the system inertia and friction. Then, the current and force start to rise to overcome the elasticity of the spring system. The installation was performed under the constant angular velocity of the DC motor.

The system is designed to enable both installation and removal of the recharging station to and from the power line. Both sequences were successfully performed and validated. In the removal sequence of the recharging station from the power line it was shown that the DC motor current is approximately constant through the entire sequence (see Figure 20).

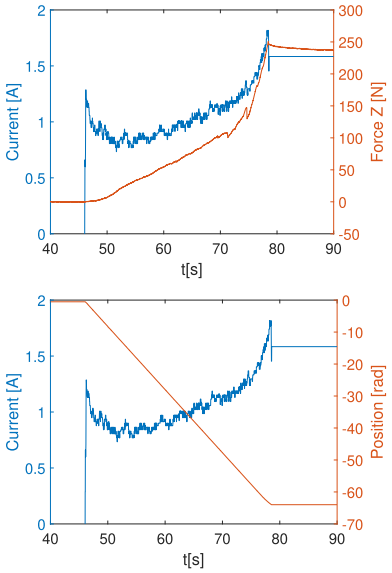

FIGURE 19. The DC motor current and force responses that occur during the recharging station installation on the power line in the trapezoidal drive shaft.

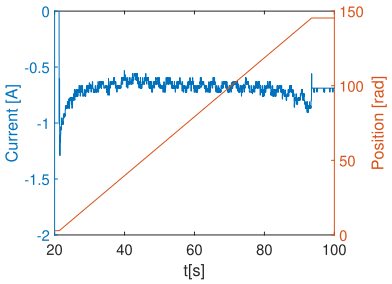

FIGURE 20. The DC motor current during the removal sequence. The graph shows that there is no significant changes in the motor current and that is kept around the constant value.

B. CHARGING CIRCUIT VALIDATION

In order to validate the model that was presented in III-A, a test setup was built to check the performances of different cores in the laboratory, as shown in Figure 21 (top). The 50 turns coil in series with a power resistor was used to generate the equivalent magnetic field of real power lines (up to 335 A). Then, the maximum power points were located by adjusting the variable resistor and reading measurement results from the power meter.

Table 6 and Figure 22 show three core types with different configurations. Figure 23 (left) shows the linear relationship between the current (from 85 A to 335 A) on the power line and harvested power. This relationship is still linear at the higher primary current (up to 823 A) according to [30]. Moreover, both graphs also show that the simulation line and experiment line are very close to each other. Likewise, Figure 23 (right) also shows the similarities between simulation and experiment results of the load voltage at maximum power point. The load voltage is nearly unchanged and almost does not depend on the primary current, as discussed in III-B2.

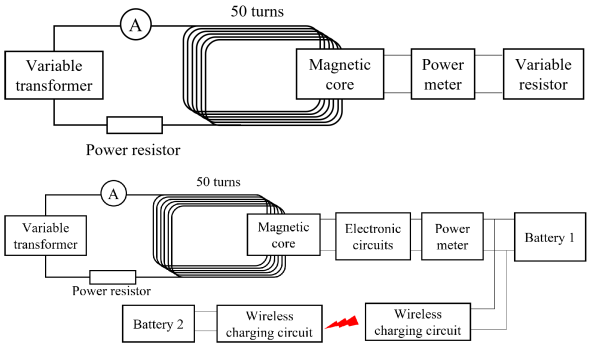

FIGURE 21. Test setup with the variable resistor (top) and electronic circuits (bottom).

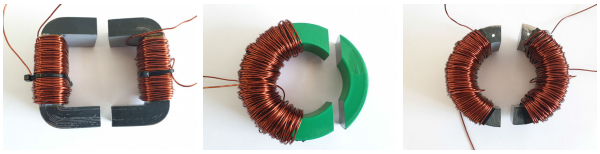

FIGURE 22. Core 1 (left), Core 2 (middle), and Core 3 (right).

TABLE 6. Parameters of 3 cores from Waasner and Hobut.

Parameter	Unit	Core 1	Core 2	Core 3
Manufacturer	-	Waasner [43]	Hobut [44]	Waasner [43]
Material	-	Silicon Steel (Si-Fe)	Silicon Steel (Si-Fe)	Silicon Steel (Si-Fe)
Core shape	-	C core	Toroidal core	Toroidal core
Weight (core + windings)	g	836	560	843
Inner diameter	mm	54	55	53
Outer diameter	mm	82	85	81
Height	mm	25	20	30
Magnetic path length (l_m)	mm	272	220	210
Cross sectional-area (A_c)	mm^2	350	300	420
Number of turns	turns	200	100	200
Maximum permeability	-	52000	7876	52000
Total air gaps	mm	0.02	0.01	0.02
Magnetic saturation	T	1.92	1.9	1.92
Estimated temperature rise at 200 A	°C	8.8	7.8	7.0

In order to see how the core shape affects the harvested power, some tests were implemented with Core 1 and 3. They have the same material from Wassner, total mass, number of turns, and temperature rise at 200 A, but different shapes and dimensions. As discussed in III-B4, more power can be harvested by using a long toroidal core instead of a short square core. As expected, in Figure 24, core 3 with the round and long shape can extract more power (16%) than core 1 with the square and short shape.

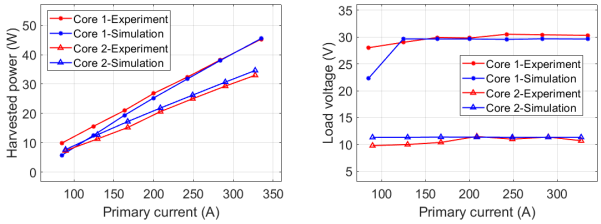

FIGURE 23. A comparison of harvested power and load voltage in simulation and experiment (Core 1 and 2).

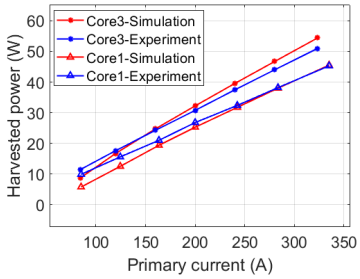

FIGURE 24. A comparison between Core 1 and Core 3 with different shapes and dimensions.

The fully electrical system in Figure 21 (bottom) was built to test in the laboratory. A rectifier and an MPPT circuit were used to track maximum power automatically and charge the battery. The wireless charging circuits still worked properly when battery 1 was being charged. The maximum charging power for battery 2 was 22 W with the efficiency of 66%. Figure 25 shows the comparison of harvested power when using the variable resistor and electronic circuits. As can be seen, less power could be extracted when testing with electronic circuits, and the efficiency was around 77% at 250 A.

Regarding the wireless charging circuits for the drone's battery, the power efficiency is calculated as follows.

$$\eta = \frac{P_{\text{out}}}{P_{\text{in}}} \times 100\%, \tag{33}$$

where P_{in} is the input power of the transmitting side (W), P_{out} is output power to the drone's battery (receiving side). The misalignment significantly affects transfer power, and maximum power can only be achieved under a certain condition. The greater the misalignment, the greater the loss of energy [45]. Some solutions for this problem were proposed, such as using multiple transmitting coils [46], moving coils [47], trapezoid shape charging station [48], etc. The commercial wireless charging circuits were used in this research. The maximum transfer power can be achieved when the transmitting and receiving coils are aligned and the distance between them is around 5 mm.

Regarding the charging circuit for the recharging station's battery, Figure 34 in the paper illustrates the comparison of extracted power with the resistive load and electronic circuits. In the case of resistive load, the authors manually adjusted the resistor to locate the maximum power point, and this is the ideal case with a unity power factor ($PF = 1$). In the

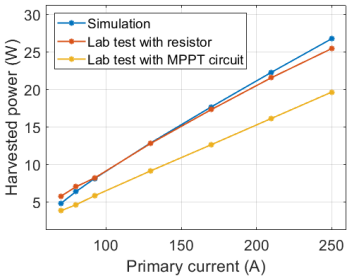

FIGURE 25. The comparison of harvested power when using the variable resistor and electronic circuits.

case of the electronic load, a MPPT circuit and rectifier were employed to find maximum power automatically. These circuits are non-linear load, and thus the power factor is reduced ($PF < 1$), or in other words, a part of power goes back to the source instead of being consumed by the load. In addition, this case also subjected to power losses on electronic components such as diodes, Mosfets, etc. Therefore, the power efficiency is calculated as follows:

$$\eta = \frac{P_{\text{ele}}}{P_{\text{res}}} \times 100\%, \tag{34}$$

where P_{res} is harvested power with the resistive load, P_{ele} is harvested power with the electronic load.

C. SYSTEM INTEGRATION

Once the mechanical and electrical design of the recharging station was completed, it was integrated into a fully functional recharging station. Prior to the actual integration, it was ensured that both the mechanical and electrical systems functioned as desired. During the design phase, the mutual physical interaction of the mechanical and electrical parts was defined. As for the magnetic core, the toroidal split-core from Hobut [44] was selected. In the recharging station, there were anticipated and manufactured predefined threaded holes for mounting the electrical compartment that houses the charging circuit (see Figure 26). Based on the specification of the used elements in creating the charging circuit, the electrical compartment was designed and developed with respect to the predefined mounting threaded holes.

On the side of the recharging station is the electronics compartment (1), which contains the complete charging circuit (see Figure 26). The split-core current transformer (2) is connected to the charging circuit, which in turn is connected to the transmitting coil. The transmitting coil is located directly under the female V-shaped landing station (3) and is connected to the charging circuit. On the other side, the receiver assembly is designed as a male V-shaped part suitable for the transmitter assembly on the recharging station and is mechanically coupled to the drone.

Another important part for wireless charging is the transmitting coil. Its placement indirectly defines the landing station of the drone. Based on the design of the recharging station, the most promising place for the drone to land is on the top of it. With the transmitting coil assembly another viable

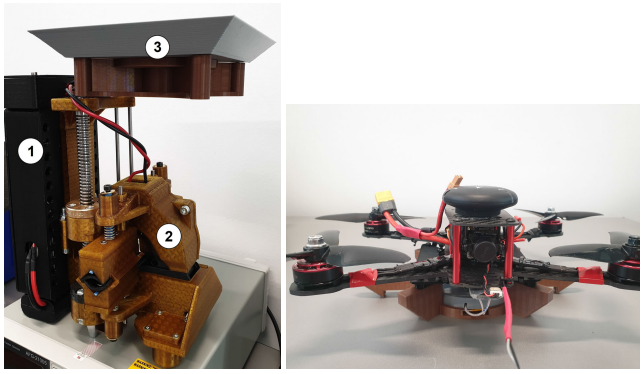

FIGURE 26. Left: The fully integrated system of the recharging station (1 - the electronics compartment; 2 - split-core current transformer; 3 - V-shaped landing station). Right: The fully integrated system of the drone HolyBro QAV250 and the receiver assembly.

part for the drone landing was the selection of the interface between the drone and the recharging station. The interface must ensure that the drone is placed firmly on the recharging station while enabling wireless charging. Having wireless charging in mind, the distance between the receiving coil on the drone and the transmitting coil on the recharging station must be suitable for maximum power transfer. Receiver and transmitter assemblies were also developed. To enable stability of the drone after landing and interaction between two coils, the above assemblies were developed as male and female V-shaped parts. This reduces the requirement to land perfectly with the drone, thus passively supporting it.

After being integrated into the recharging station, the internal and drone batteries were charged to test the electronic circuits. In order to extend the lifespan, the batteries should be charged from 20% to only 80%. Both batteries were charged at the same time and the charging time for the drone battery (LiPo 3S, 3000 mAh) was 70 minutes with the maximum wireless charging power of 22 W (Figure 27). The flight time depends on various factors such as the drone's weight and size, battery capacity, payload weight, operating modes, wind disturbance, etc. In this paper, the HolyBro QAV250 drone with a 420 g payload was used, and the flight time is approximately 15 minutes. This drone is able to carry a 500 g payload, and the detailed payload is shown in Table 7.

TABLE 7. Detailed payload of the HolyBro QAV250 drone.

Payload	Weight (g)
Battery LiPo 3S 3000 mAh	211
Power meter	86
Charging circuit	52
Charging dock	71
TOTAL WEIGHT	**420**

D. POWER LINE CHARGING

In this experiment, the electromechanical functionality of the recharging station is checked. As for the electrical part of the recharging station, the charging circuit was validated on the actual power line. On the other hand, the stability of the

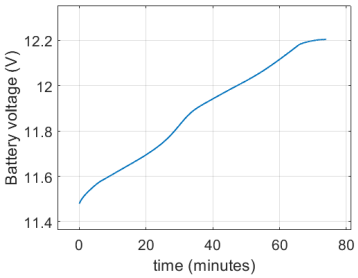

FIGURE 27. The charging time of the drone battery.

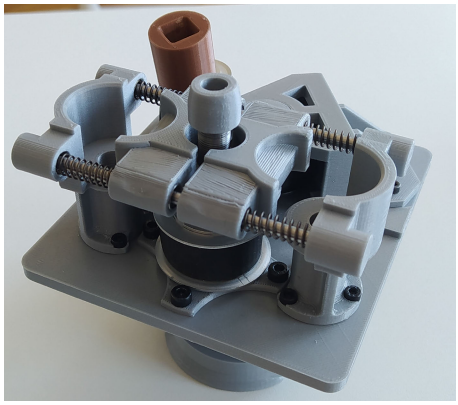

FIGURE 28. Robot end effector for the installation and the removal of the recharging station.

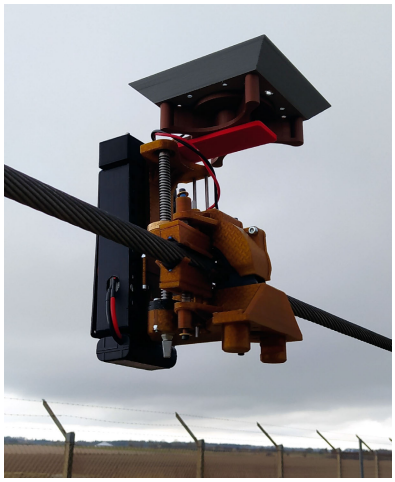

FIGURE 29. The recharging station installed on the power line at the airport on the real power line setup.

recharging station was demonstrated during the robot installation. However, since the real environment presents many challenges to make the recharging station work as desired, the experiment of power transmission of the recharging station from the power line was conducted at the H.C. Andersen Airport (Odense, Denmark) on real power transmission lines with two towers of 10 m in height. After installing the recharging station on the cable, the primary current was adjusted and the charging power was checked. In Figure 30,

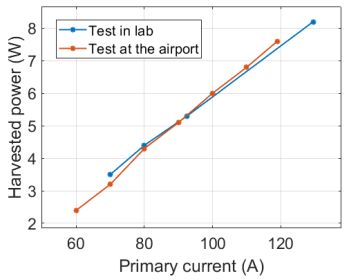

FIGURE 30. The comparison of harvested power in the laboratory and at the airport.

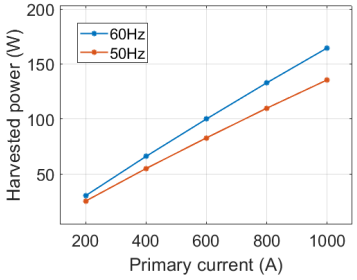

FIGURE 31. The comparison of extracted power between 50 Hz and 60 Hz power line.

the similarity between the test results in the laboratory and at the airport is clearly seen.

For the effects of the operating frequency, according to [42], silicon steel works well with a 400 Hz power line. Therefore, the magnetic core is able to operate with a 60 Hz power line. In addition, the higher frequency, the more power can be extracted. Figure 31 shows the simulation results that compare the harvested power of the same magnetic core (Core 1 - Table 6) at different operating frequencies (i.e., 50 Hz and 60 Hz). It can be seen that extra 20% power can be harvested with a 60 Hz power line.

For the effects of high voltage cables, the recharging station aims to be installed up to a 15 kV power line. However, the impact of high voltage on the operation of the recharging station is not the primary focus of this paper. The real power line at the H.C. Andersen airport is low voltage and has no impact on the performance of electronic circuits. For the sake of clarity and without losing generality, a detailed analysis of the EMI effect on drone electronics was presented in the authors' previous work [49]. The shielded drone was tested with 400 kV cables without any difficulties. In the future work, the shielded recharging station will be developed.

V. CONCLUSION

The objective of this research work within the project AERIAL CORE is to develop a recharging station capable of harvesting energy from the power line and transmitting it to the landed drone, thus ensuring greater autonomy of the drones in the power line environment. This paper presents the electromechanical design of the recharging station, which can be installed and removed remotely using the aerial manipulator system and a special robot end effector that enables aerial manipulation of the recharging station. The installation and removal of the recharging station using the developed robot end effector was demonstrated and confirmed. In addition, the mechanical and electrical design of the recharging station were successfully integrated and tested indoors and outdoors, validating the charging circuit and charging via the power line. In addition, the conducted experiments have shown that the recharging station can be installed and removed from the power line using a special robot end effector, and that wireless power transmission is possible in both a controlled and real-world environment. The results show tremendous potential for ensuring drone autonomy in power line inspection and monitoring. Future focus will be on refining the landing station and demonstrating drone landing. Eventually, the drone landing is to be fully autonomous with use of a visual or magnetic feedback [50], [51]. Initial experiments on manual drone landing provided valuable insights, and a new landing station design that completely eliminates misalignment is being considered. However, the main focus of this research was to demonstrate and validate the operation of the recharging station and installation using the robotic arm and a special robot end effector.

ACKNOWLEDGMENT

The authors would like to thank Nicolaj Haarhøj Malle, Frederik Falk Nyboe, and Oscar Bowen Schofield from the SDU UAS Centre, MMMI, University of Southern Denmark, for their assistance during system integration activities and for technical support in preparing and navigating the UAV system during the experimental procedures and also would like to thank Prof. Matko Orsag (an Associate Professor), Ph.D. work from LARICS, University of Zagreb, for assistance in illustrating the described AERIAL CORE project task, shown as Figure 1.

REFERENCES

[1] T. Disyadej, J. Promjan, K. Poochinapan, T. Mouktonglang, S. Grzybowski, and P. Muneesawang, "High voltage power line maintenance & inspection by using smart robotics," in *Proc. IEEE Power Energy Soc. Innov. Smart Grid Technol. Conf. (ISGT)*, Feb. 2019, pp. 31–34.

[2] P. B. Wale and K. K. Sandeep, "Maintenance of transmission line by using robot," in *Proc. Int. Conf. Autom. Control Dyn. Optim. Techn. (ICACDOT)*, Sep. 2016, pp. 538–542.

[3] N. Pouliot and S. Montambault, "Geometric design of the LineScout, a teleoperated robot for power line inspection and maintenance," in *Proc. IEEE Int. Conf. Robot. Autom.*, May 2008, pp. 3970–3977.

[4] F. Ruggiero, V. Lippiello, and A. Ollero, "Aerial manipulation: A literature review," *IEEE Robot. Autom. Lett.*, vol. 3, no. 3, pp. 1957–1964, Jul. 2018.

[5] M. Orsag, C. Korpela, P. Oh, and S. Bogdan, *Aerial Manipulation*. Cham, Switzerland: Springer, 2018. [Online]. Available: https://link.springer.com/book/10.1007/978-3-319-61022-1#bibliographic-information

[6] X. Meng, Y. He, and J. Han, "Survey on aerial manipulator: System, modeling, and control," *Robotica*, vol. 38, no. 7, pp. 1288–1317, Jul. 2020.

[7] A. Ollero, M. Tognon, A. Suarez, D. Lee, and A. Franchi, "Past, present, and future of aerial robotic manipulators," *IEEE Trans. Robot.*, vol. 38, no. 1, pp. 626–645, Feb. 2022.

[8] A. Gohari, A. B. Ahmad, R. B. A. Rahim, A. S. M. Supa'at, S. A. Razak, and M. S. M. Gismalla, "Involvement of surveillance drones in smart cities: A systematic review," *IEEE Access*, vol. 10, pp. 56611–56628, 2022.

[9] M. A. Hoque, M. Hossain, S. Noor, S. M. R. Islam, and R. Hasan, "IoTaaS: Drone-based Internet of Things as a service framework for smart cities," *IEEE Internet Things J.*, vol. 9, no. 14, pp. 12425–12439, Jul. 2022.
[10] D. Darsena, G. Gelli, I. Iudice, and F. Verde, "Detection and blind channel estimation for UAV-aided wireless sensor networks in smart cities under mobile jamming attack," *IEEE Internet Things J.*, vol. 9, no. 14, pp. 11932–11950, Jul. 2022.
[11] J. Cacace, S. M. Orozco-Soto, A. Suarez, A. Caballero, M. Orsag, S. Bogdan, G. Vasiljevic, E. Ebeid, J. A. A. Rodriguez, and A. Ollero, "Safe local aerial manipulation for the installation of devices on power lines: AERIAL-CORE first year results and designs," *Appl. Sci. Switzerland*, vol. 11, no. 13, pp. 1–19, 2021.
[12] M. C. Achtelik, J. Stumpf, D. Gurdan, and K.-M. Doth, "Design of a flexible high performance quadcopter platform breaking the MAV endurance record with laser power beaming," in *Proc. IEEE/RSJ Int. Conf. Intell. Robots Syst.*, Sep. 2011, pp. 5166–5172.
[13] K.-R. Li, K.-Y. See, W.-J. Koh, and J.-W. Zhang, "Design of 2.45 GHz microwave wireless power transfer system for battery charging applications," in *Proc. Prog. Electromagn. Res. Symp. Fall (PIERS-FALL)*, 2017, pp. 2417–2423.
[14] D. H. Nguyen, S. Suganuma, K. Shimamura, and K. Mori, "Millimeter wave power transfer to an autonomously controlled micro aerial vehicle," *Trans. Jpn. Soc. Aeronaut. Space Sci.*, vol. 63, no. 3, pp. 101–108, 2020.
[15] T. M. Mostafa, A. Muharam, and R. Hattori, "Wireless battery charging system for drones via capacitive power transfer," in *Proc. IEEE PELS Workshop Emerg. Technol., Wireless Power Transf. (WoW)*, May 2017, pp. 1–6.
[16] S. Aldhaher, P. D. Mitcheson, J. M. Arteaga, G. Kkelis, and D. C. Yates, "Light-weight wireless power transfer for mid-air charging of drones," in *Proc. 11th Eur. Conf. Antennas Propag. (EUCAP)*, Mar. 2017, pp. 336–340.
[17] J. M. Arteaga, S. Aldhaher, G. Kkelis, C. Kwan, D. C. Yates, and P. D. Mitcheson, "Dynamic capabilities of multi-MHz inductive power transfer systems demonstrated with batteryless drones," *IEEE Trans. Power Electron.*, vol. 34, no. 6, pp. 5093–5104, Jun. 2018.
[18] C. Bil, M. Simic, and V. Vojisavljevic, "Design of a recharge station for UAVs using non-contact wireless power transfer," in *Proc. 54th AIAA Aerosp. Sci. Meeting*, Jan. 2016, p. 1525.
[19] C. Wang and Z. Ma, "Design of wireless power transfer device for UAV," in *Proc. IEEE Int. Conf. Mechtron. Autom.*, Aug. 2016, pp. 2449–2454.
[20] S. Obayashi, Y. Kanekiyo, H. Uno, T. Shijo, K. Sugaki, H. Kusada, H. Nakakoji, Y. Hanamaki, and K. Yokotsu, "400-W UAV/drone inductive charging system prototyped for overhead power transmission line patrol," in *Proc. IEEE Wireless Power Transf. Conf. (WPTC)*, Jun. 2021, pp. 1–3.
[21] F. Guo, H. Hayat, and J. Wang, "Energy harvesting devices for high voltage transmission line monitoring," in *Proc. IEEE Power Energy Soc. General Meeting*, Jul. 2011, pp. 1–8.
[22] V. Gupta, A. Kandhalu, and R. Rajkumar, "Energy harvesting from electromagnetic energy radiating from AC power lines," in *Proc. 6th Workshop Hot Topics Embedded Networked Sensors (HotEmNets)*, 2010, pp. 1–6.
[23] J. Moon, J. Donnal, J. Paris, and S. B. Leeb, "VAMPIRE: A magnetically self-powered sensor node capable of wireless transmission," in *Proc. 28th Annu. IEEE Appl. Power Electron. Conf. Expo. (APEC)*, Mar. 2013, pp. 3151–3159.
[24] J. Ahola, T. Ahonen, V. Sarkimaki, A. Kosonen, J. Tamminen, R. Tiainen, and T. Lindh, "Design considerations for current transformer based energy harvesting for electronics attached to electric motor," in *Proc. Int. Symp. Power Electron., Electr. Drives, Autom. Motion*, Jun. 2008, pp. 901–905.
[25] R. Wang, Z. Wang, J. Du, J. Wu, and X. He, "Design considerations of maximum energy harvesting and voltage control from high voltage power cables," in *Proc. Int. Power Electron. Appl. Conf. Expo.*, Nov. 2014, pp. 920–923.
[26] S. A. A. Najafi, A. A. Ali, Y. Sozer, and A. De Abreu-Garcia, "Energy harvesting from overhead transmission line magnetic fields," in *Proc. IEEE Energy Convers. Congr. Expo. (ECCE)*, Sep. 2018, pp. 7075–7082.
[27] G. Gruber, M. Neumayer, T. Bretterklieber, A. Siegl, and R. Felsberger, "Miniaturized magnetic energy harvester: Lightweight and safe transformer design," in *Proc. IEEE Int. Instrum. Meas. Technol. Conf. (IMTC)*, May 2021, pp. 1–6.
[28] R. Kitchen, N. Bierwolf, S. Harbertson, B. Platt, D. Owen, K. Griessmann, and M. A. Minor, "Design and evaluation of a perching hexacopter drone for energy harvesting from power lines," in *Proc. IEEE/RSJ Int. Conf. Intell. Robots Syst. (IROS)*, Oct. 2020, pp. 1192–1198.
[29] J. D. Boles, B. Ozpineci, L. M. Tolbert, T. A. Burress, C. W. Ayers, and J. A. Baxter, "Inductive power harvesting for a touchless transmission line inspection system," in *Proc. IEEE Power Energy Soc. Gen. Meeting (PESGM)*, Jul. 2016, pp. 1–5.
[30] N. Iversen, O. B. Schofield, L. Cousin, N. Ayoub, G. vom Bogel, and E. Ebeid, "Design, integration and implementation of an intelligent and self-recharging drone system for autonomous power line inspection," in *Proc. IEEE/RSJ Int. Conf. Intell. Robots Syst. (IROS)*, Sep. 2021, pp. 4168–4175.
[31] N. Iversen, A. Kramberger, O. B. Schofield, and E. Ebeid, "Novel power line grasping mechanism with integrated energy harvester for UAV applications," in *Proc. IEEE Int. Symp. Saf., Secur., Rescue Robot. (SSRR)*, Oct. 2021, pp. 34–39.
[32] G. vom Bogel, L. Cousin, N. Iversen, E. S. M. Ebeid, and A. Hennig, "Drones for inspection of overhead power lines with recharge function," in *Proc. 23rd Euromicro Conf. Digit. Syst. Design (DSD)*, Aug. 2020, pp. 497–502.
[33] R. Miller, F. Abbasi, and J. Mohammadpour, "Power line robotic device for overhead line inspection and maintenance," *Ind. Robot, Int. J.*, vol. 44, no. 1, pp. 75–84, Jan. 2017.
[34] M. F. M. Campos, G. A. S. Pereira, S. R. C. Vale, A. Q. Bracarense, G. A. Pinheiro, and M. P. Oliveira, "A mobile manipulator for installation and removal of aircraft warning spheres on aerial power transmission lines," in *Proc. IEEE Int. Conf. Robot. Autom.*, May 2002, pp. 3559–3564.
[35] D. Yang, Z. Feng, X. Ren, and N. Lu, "A novel power line inspection robot with dual-parallelogram architecture and its vibration suppression control," *Adv. Robot.*, vol. 28, no. 12, pp. 807–819, Jun. 2014.
[36] F. Yu, W. Kai, and W. Shaolei, "Design of clamping device for overhead line branch line with live installation," in *Proc. Int. Conf. Artif. Intell. Electromech. Automat. (AIEA)*, 2020, pp. 321–324.
[37] M. Jayatilaka, M. Shanmugavel, and S. V. Ragavan, "Robonwire: Design and development of a power line inspection robot," in *Proc. 1st Int. 16th Nat. Conf. Mach. Mech.*, 2013, pp. 1–8.
[38] B. V. Vidyadhara, L. A. Tony, M. S. Gadde, S. Jana, V. P. Varun, A. A. Bhise, S. Sundaram, and D. Ghose, "Design and integration of a drone based passive manipulator for capturing flying targets," *Robotica*, vol. 40, no. 7, pp. 2349–2364, Jul. 2021.
[39] C. W. T. McLyman, *Transformer and Inductor Design Handbook*. Boca Raton, FL, USA: CRC Press, Dec. 2017.
[40] *Soft Magnetic*. Accessed: May 16, 2022. [Online]. Available: https://www.carpentertechnology.com/
[41] *Soft Magnetic Materials and Stamped Parts*. Accessed: May 15, 2022. [Online]. Available: https://vacuumschmelze.com/
[42] *Magnetic Cores*. Accessed: May 16, 2022. [Online]. Available: https://www.tct-magnetic.com/
[43] *Transformatorenbauteile*. Accessed: May 10, 2022. [Online]. Available: http://www.waasner.de/
[44] *Current Transformer*. Accessed: May 19, 2022. [Online]. Available: https://www.hobut.co.uk/
[45] Y. Gao, A. Ginart, K. B. Farley, and Z. T. H. Tse, "Misalignment effect on efficiency of wireless power transfer for electric vehicles," in *Proc. IEEE Appl. Power Electron. Conf. Expo. (APEC)*, Mar. 2016, pp. 3526–3528.
[46] T. Campi, S. Cruciani, and M. Feliziani, "Wireless power transfer technology applied to an autonomous electric UAV with a small secondary coil," *Energies*, vol. 11, no. 2, p. 352, Feb. 2018.
[47] C. H. Choi, H. J. Jang, S. G. Lim, H. C. Lim, S. H. Cho, and I. Gaponov, "Automatic wireless drone charging station creating essential environment for continuous drone operation," in *Proc. Int. Conf. Control, Autom. Inf. Sci. (ICCAIS)*, Oct. 2016, pp. 132–136.
[48] S. Obayashi, Y. Kanekiyo, and T. Shijo, "UAV/drone fast wireless charging FRP frustum port for 85-kHz 50-V 10-A inductive power transfer," in *Proc. IEEE Wireless Power Transf. Conf. (WPTC)*, Nov. 2020, pp. 219–222.
[49] M. Skriver, A. Stengaard, U. P. Schultz, and E. Ebeid, "Experimental investigation of EMC weaknesses in UAVs during overhead power line inspection," in *Proc. Int. Conf. Unmanned Aircr. Syst. (ICUAS)*, Jun. 2022, pp. 626–635.
[50] G. Vasiljevic, D. Martinovic, M. Batos, and S. Bogdan, "Validation of two-wire power line UAV localization based on the magnetic field strength," 2022, *arXiv:2206.09169*.
[51] D. Martinović, S. Bogdan, and Z. Kovačić, "Mathematical considerations for unmanned aerial vehicle navigation in the magnetic field of two parallel transmission lines," *Appl. Sci.*, vol. 11, no. 8, p. 3323, Apr. 2021. [Online]. Available: https://www.mdpi.com/2076-3417/11/8/3323

DARIO STUHNE (Graduate Student Member, IEEE) was born in Zagreb, Croatia, in 1996. He received the bachelor's degree *(magna cum laude)* and the master's degree *(magna cum laude)* in mechanical engineering specialized in product design and development from the Faculty of Mechanical Engineering and Naval Architecture, University of Zagreb, in 2019 and 2020, respectively. He is currently pursuing the Ph.D. degree in control engineering and automation with the University of Zagreb.

In 2021, he joined the Laboratory for Robotics and Intelligent Control Systems, Faculty of Electrical Engineering and Computing, University of Zagreb, as a Research Associate. His research interests include design and development of robotic systems.

VIET DUONG HOANG received the bachelor's and master's degrees in electrical engineering from the Hanoi University of Science and Technology, Vietnam, in 2016 and 2020, respectively. He is currently pursuing the Ph.D. degree with the UAS Center, University of Southern Denmark. His research interests include energy harvesting and power line inspection using drones.

GORAN VASILJEVIC (Member, IEEE) received the master's degree in electrical engineering, in 2009, and the Ph.D. degree, in 2017. His Ph.D. thesis titled "Highly Accurate Markerless Localization of Mobile Robots in Indoor Industrial Environments." He is currently a Postdoctoral Researcher with the Laboratory for Robotics and Intelligent Control Systems (LARICS), Faculty of Electrical Engineering and Computing, University of Zagreb. He has more than 25 publications (book chapters, journal articles, and conference papers). He has been involved in several Croatian and international scientific and research projects and industrial cooperation projects.

STJEPAN BOGDAN (Senior Member, IEEE) received the Ph.D. degree in EE from the University of Zagreb, Croatia, in 1999. Currently, he is a Full Professor at the Laboratory for Robotics and Intelligent Control Systems (LARICS), Faculty of Electrical Engineering and Computing, University of Zagreb. He is the coauthor of four books and has published more than 200 conferences and journal articles. His research interests include autonomous systems, aerial robotics, multi-agent systems, intelligent control, and discrete event systems. He was a Program Committee and an Organizing Committee Member of major IEEE Control and Robotics Conferences. He served as an Associate Editor of IEEE TRANSACTIONS ON AUTOMATION SCIENCE AND ENGINEERING.

ZDENKO KOVACIC (Senior Member, IEEE) is currently a Full Professor at the Faculty of Electrical Engineering and Computing, University of Zagreb, and the Head of the Laboratory for Robotics and Intelligent Control Systems (LARICS). He spent 1990 and 1991 as an IREX Visiting Researcher at the Bradley Department of Electrical Engineering, the Virginia Polytechnic Institute, and the State University, Blacksburg, USA. He has authored three books in the areas of robotics, manufacturing systems, and intelligent control. He has more than 200 scientific publications (book chapters, journal articles, and conference papers). He has been the principal investigator of more than 40 successfully completed international and Croatian research and development projects. Currently, he is the Leader of three Research and Development Projects with industrial partners, the Coordinator and the Team Leader of two ESIF-funded Research and Development Projects, and a Collaborator on several ongoing Horizon 2020 projects. In 2013, he was awarded the "Fran Bošnjaković" prize by the University of Zagreb. He was a recipient of the Faculty of Electrical Engineering and Computing "Josip Lončar" Award, in 2018. In 2005 and 2010, he was the President of Croatian Robotics Society. In 2012 and 2015, he was the President-Elect of Croatian Robotic Association.

ANIBAL OLLERO (Fellow, IEEE) is currently a Full Professor and the Head of the GRVC Robotics Laboratory with 75 members and the Robotics and Intelligent Systems Institute, University Seville, and the Scientific Advisor of the Center for Aerospace Technologies (CATEC), Seville. He has been a Full Professor at the University of Santiago and the University of Malaga, Spain, and a Researcher with the Robotics Institute, Carnegie Mellon University, Pittsburgh, USA, and LAAS-CNRS, Toulouse, France. He has authored more than 800 publications, including nine books and more than 235 articles in journals, and has been an editor of 15 books. He led more than 160 research projects, participating in more than 41 projects of the European research programs, being coordinator of seven. He has been recognized with 28 awards, including the Spanish National Research Award in Engineering, the Rei Jaume I in New Technologies, the Andalusia Award to the Engineering Development, the Overall Information and Communication Technologies Innovation Radar Prize 2017 of the European Commission, and several best paper awards in conferences. He also was the Coordinator of the team that won the Challenge three of the MBZIRC 2020 International Robotics Competition.

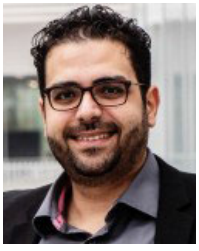

EMAD SAMUEL MALKI EBEID (Senior Member, IEEE) received the Ph.D. degree in distributed embedded systems from the University of Verona, Italy, with a European Doctorate Label, in 2014. He is currently an Associate Professor and the Leader of the DIII Research Group, University of Southern Denmark. He has published more than 70 articles in flagship journals and conferences in robotics and embedded systems. His research interests include autonomous drone system design for infrastructure inspection and interaction utilizes cutting-edge technologies (MPSoCs and FPGAs) to build an advanced reconfigurable onboard unit for controling the drone in real-time to detect and grasp the powerlines for inspection and recharging applications. He is the Coordinator of the EU H2020 Drones4Safety and Innovation Fund Grand Solutions Drones4Energy projects.